Optics Letters

High-resolution phase-sensitive sum frequency generation spectroscopy by time-domain ptychography

Tobias Schweizer,[1] Bruno G. Nicolau,[2] Priscila Cavassin,[2] Thomas Feurer,[1] Natalie Banerji,[2] and Julien Réhault[2,*]

[1]Institute of Applied Physics, University of Bern, Sidlerstrasse 5, 3012 Bern, Switzerland
[2]Department of Chemistry and Biochemistry, University of Bern, Freiestrasse 3, 3012 Bern, Switzerland
*Corresponding author: julien.rehault@dcb.unibe.ch

Received 22 July 2020; revised 11 September 2020; accepted 12 September 2020; posted 17 September 2020 (Doc. ID 403339); published 1 November 2020

We demonstrate that time-domain ptychography, when applied to a set of broadband vibrational sum frequency spectra, reconstructs amplitude and phase of the vibrational free induction decay from an interfacial sample with a resolution that is independent of up-converting pulse bandwidth and spectrometer resolution. These important improvements require no modifications to most standard homodyne setups, and the method is applicable to other coherent homodyne spectroscopies such as coherent anti-Stokes Raman spectroscopy and transient grating spectroscopy.

https://doi.org/10.1364/OL.403339

Sum frequency generation spectroscopy (SFG) is a method of choice to selectively investigate surfaces or interfaces [1]. In particular, vibrational SFG (vSFG) is used to study vibrational modes of interfacial molecules, providing structural and orientational information with sub-monolayer sensitivity. In the broadband version of vSFG (BB-vSFG) a narrowband near-infrared (NIR) pulse is mixed with a broadband IR pulse that spans all vibrational frequencies of interest. The resulting sum-frequency signal from the interface is emitted in the phase matching direction (see Fig. 1), and its spectral intensity I_{SFG} is typically measured with an array detector:

$$I_{\mathrm{SFG}}(\omega_{\mathrm{SFG}}, \tau) \propto |E_{\mathrm{SFG}}(\omega_{\mathrm{SFG}}, \tau)|^2, \quad (1)$$

where $\omega_{\mathrm{SFG}} = \omega_{\mathrm{NIR}} + \omega_{\mathrm{IR}}$ is the sum frequency of the NIR and IR pulses at frequencies ω_{NIR} and ω_{IR}, respectively. The time delay τ is selected so that the NIR probe and IR induced polarization overlap in time, but its exact value is somewhat arbitrary. Since the spectrum results from a homodyne measurement, it contains only information on the vibrational amplitudes, and phase information is lost. Yet, accessing the complex field $E_{\mathrm{SFG}}(\omega_{\mathrm{SFG}})$, specifically its phase, is crucial in order to determine correctly vibrational lineshapes or absolute orientations of interfacial molecules [2–8]. Hence, quite some effort has been dedicated to the development of phase-sensitive SFG (PS-SFG) modalities [8–16] which all rely on heterodyning the SFG signal with a local oscillator or the non-resonant background (NRB) signal arising in some configurations[17,18]. These schemes successfully recover the complex field but come at the expense of a more complex experimental apparatus. In this Letter, we demonstrate reconstruction of phase information from a series of homodyne measurements via time-domain ptychography [19], which requires no modification to a standard experimental setup. An algorithm is applied to a set of spectra measured at different time delays τ and reconstructs the complex linear vibrational polarization $P_S^{(1)}(t)$ from the interface. Moreover, we show that, in contrast to standard homodyne BB-vSFG measurements, the resolution of the reconstructed polarization is no longer limited by the spectrometer nor by the NIR bandwidth, but only by the largest delay τ. Thus, any standard homodyne BB-vSFG setup can produce phase information with unprecedented spectral resolution if a handful of spectra are measured at different delays τ and post-processed via time-domain ptychography. We named the new method HIPPY, for HIgh-resolution Phase-sensitive spectroscopy with PtYchography.

Time-domain ptychography is an emerging technique for phase and amplitude characterization of ultrashort coherent laser pulses [19]. In its basic implementation it uses the ptychographic iterative engine (PIE) to reconstruct a complex object pulse from a set of sum-frequency spectra that results from the mixing of a well-characterized probe pulse with an unknown complex object pulse at different delays between the two (see Fig. 1) [19]. Briefly, the algorithm starts with a random complex object pulse as an initial guess (see Fig. 1), and in every iteration, all measured spectra are processed. The algorithm calculates the product field for a particular time delay from the probe and the current estimate of the object pulse, calculates its Fourier transform, and replaces its modulus by the square root of the measured spectrum while preserving its phase. After an inverse Fourier transformation, the difference between the new and old product fields is used to update the current estimate of the object pulse. The best approximation to the actual object pulse appears typically after only a few iterations [20,21]. Time-domain ptychography has been successfully used to characterize

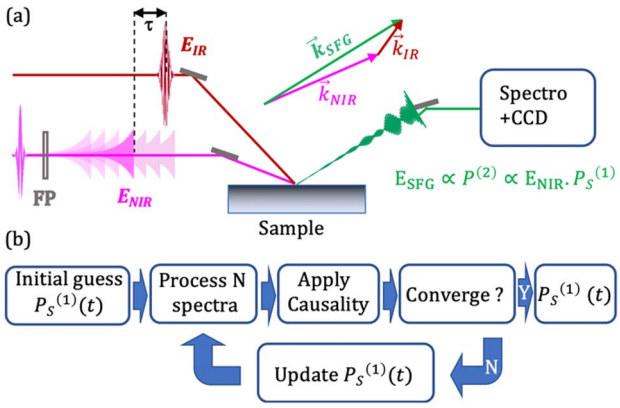

Fig. 1. (a) Experimental setup for BB-vSFG with an asymmetric probe pulse created via a Fabry–Perot étalon. E_{NIR}, E_{IR}, and E_{SFG} represent the fields of all pulses involved in the experiment, with their phase matching conditions. (b) PIE scheme for the reconstruction of complex objects, here, $P_S^{(1)}(t)$.

attosecond and supercontinuum pulses [19,22–25], and the robustness of PIE has been demonstrated both theoretically and experimentally [26,27].

In a typical BB-vSFG setup, a narrowband NIR pulse is mixed with a broadband IR pulse that covers all molecular vibrations of interest, typically between 800 and 4000 cm^{-1}. The center wavelength of the NIR pulse is selected such that the sum-frequency signal appears in a wavelength range that can be conveniently detected by silicon technology. Its bandwidth, which determines the resolution of the recorded vibrational spectra, is typically adjusted via spectral filtering with bandpass interference filters, Fabry–Perot étalons, or zero-dispersion monochromators. In the impulsive limit of BB-vSFG, where the IR pulse is assumed to be short compared to the polarization, the signal field E_{SFG} is proportional to second-order polarization and can be approximated as [28,29]

$$E_{SFG}(t,\tau) \propto P^{(2)}(t) \propto E_{NIR}(t-\tau)\, P_S^{(1)}(t), \quad (2)$$

where $E_{NIR}(t-\tau)$ is the time delayed NIR pulse, and $P_S^{(1)}(t)$ is the surface linear vibrational polarization or free induction decay (FID) resulting from the interaction between the molecular sample through its complex linear susceptibility $\chi^{(1)}$ and the IR pulse $E_{IR}(t)$. Hereafter, we will use PIE notation and associate the $E_{NIR}(t-\tau)$ pulse with the probe and the polarization $P_S^{(1)}(t)$ with the complex object to be reconstructed. To apply HIPPY to SFG, we have to measure a set of homodyne SFG spectra for different time delays τ.

In our setup sketched in Fig. 1(a), the NIR probe pulse is generated by passing a 100 fs pulse at 800 nm through a thin air-spaced Fabry–Perot étalon. The resulting narrowband probe is a time asymmetric pulse with a sharp rise and slow exponential decay. Such probe pulses are conveniently used for mixing with long FIDs while removing the NRB that can arise from the overlap between NIR and IR pulses [30]. Here, the IR pulse was centered at 3.3 μm, corresponding to the energy of C-H stretch mode, and had a bandwidth of 240 nm (200 cm^{-1}). The probe pulse displayed in Fig. 2(b) is calculated from the laser and Fabry–Perot parameters, but also characterized with the integrated intensity of the SFG signal, which is dominated by the NRB and reflects the cross correlation between the NIR and IR pulses. The probe pulse can be delayed relative to the IR pulse via a mechanical translation stage. The sum-frequency spectra were recorded with a Kymera 193 spectrometer with a 1200 l/mm grating blazed at 600 nm combined with an Andor Idus 420 camera giving a spectral resolution of better than 7 cm^{-1} at 640 nm. For experimental demonstration, we used a monolayer of octadecanethiol (ODT) on gold [31].

We measured seven spectra with a delay increment of 400 fs, and the spectral intensities between 2820 and 3020 cm^{-1} are displayed in Fig. 2(a) (see Data File 1, Data File 2, and Data File 3 [32]). The first two spectra exhibit a strong NRB contribution due to the gold substrate, which is nearly suppressed after delay #3. Also, the shape and intensity of the spectra and the vibrational signatures contained in them depend substantially on the time delay τ. While in standard BB-vSFG, this constitutes a major obstacle for the correct interpretation of data, here, all spectra are crucial as input for HIPPY.

The probe pulse and the seven spectra shown in Fig. 2(a) were subsequently used as input to the PIE algorithm (see Code 1, Ref. [33]). After every update, the actual object, i.e., FID, was multiplied with the window function shown in Fig. 2(b) to remove noise in regions where no signal is expected. Typically, after only a few tens of iterations (about 1 s computation time), the algorithm had converged and reconstructed the spectra displayed in the lower panel of Fig. 2(a). Despite some minor discrepancies, the overall shape and magnitude of the spectra at different time delays are very well reproduced. The recovered vibrational FID is displayed in Fig. 2(b) and is Fourier transformed to extract amplitude and phase of the frequency dependent signal. Note that absolute as well as linear phase (absolute time delay) cannot be recovered and would need additional reference measurements [34–36]. Therefore, we chose an arbitrary offset so that the phase is zero at the maximum amplitude and subtracted a linear phase so that the remaining phase is flattest for the spectral window considered. Here, only seven spectra were sufficient for a high-fidelity reconstruction, but we can easily include more spectra combined with a smaller time delay increment to improve the results, especially when the signal-to-noise ratio is lower. The spectral amplitude in Fig. 2(c) is dominated by a strong NRB, and the vibrational signatures from the ODT monolayer appear as dips in the NRB envelope.

Four important points are worth emphasizing. First, the retrieved signal does not depend on the shape of the NIR probe pulse. Second, the windowing effect in standard vSFG due to the finite duration of the NIR pulse is eliminated, as the total time window is now determined by the number of recorded spectra times the time delay increment. Third, and this is a consequence of the previous points, the spectral resolution of the recovered signal is not limited anymore by the duration of the NIR pulse nor by the spectrometer resolution. To illustrate this, we compare the square root of the spectrum measured at the first time delay with the reconstructed amplitude in Fig. 2(c). Clearly, the reconstructed amplitude shows much better resolved vibrational modes and in fact now reveals their true lineshape. The improvement comes from the fact that time-domain ptychography merges the best of the frequency domain approach, i.e., acquiring highly resolved spectra at each acquisition with a sensitive CCD detector, together with the flexibility of the time-domain approach, i.e., increasing the scan range by recording spectra at more and more time delays. Fourth, in BB-vSFG, we typically must find a compromise between spectral resolution and signal strength. A longer probe permits a better resolution (if not limited by the spectrometer) but at the same

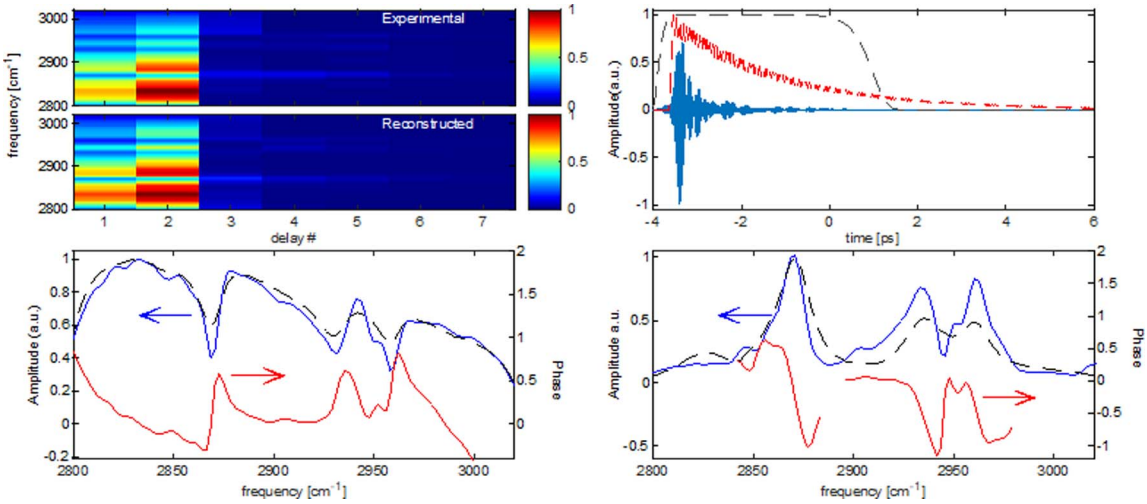

Fig. 2. (a) Top: intensity plot of measured spectra for different delays separated by 400 fs. Bottom: corresponding reconstructed spectra. (b) Reconstructed FID (blue), probe pulse (red), and window function (dashed black curve) used for noise suppression. (c) Amplitude (blue) and phase (red) of reconstructed FID and the square root of the experimental spectrum for the first delay (dashed black curve). (d) Amplitude (blue) and phase (red) of $P_S^{(1)}$ after NRB subtraction and the square root of the experimental spectrum for the fourth delay (dashed black curve).

time lowers the signal strength [3,8,37,38]. To circumvent this, alternative time-domain techniques have been suggested. In our approach, this is no longer an issue, and we can easily use shorter probe pulses yielding higher signal strengths without sacrificing spectral resolution as long as we record enough spectra to cover the entire FID. Finally, we would like to comment on the NRB. For the data presented in Fig. 2(c), we chose to use all seven spectra, including the first two, which feature a substantial NRB from the gold surface. Since HIPPY reconstructs whatever part of the object is scanned by the time-delayed probe pulses, we may in principle select only spectra taken at delays with a negligible NRB contribution (here, after delay #4, see Fig. S.1, Supplement 1, for illustration). Alternatively, we can remove the NRB after the reconstruction. The latter is advantageous since the NRB heterodynes part of the signal, and including the spectra with substantial NRB helps to improve the retrieval of the FID. To illustrate this, we subtracted the NRB from the FID, by fitting the NRB envelope and phase [assuming it to be flat in the middle of the spectrum of Fig. 2(c); see also Fig. S.2, Supplement 1]. In Fig. 2(d), we show the resulting amplitude and phase of the FID that reflects now only the response from the ODT monolayer. The phase is displayed only where the amplitude is higher than 3% of the maximal amplitude. For comparison, we included the square root of the spectrum measured at the fourth delay, which is the first without NRB contribution. The comparison reveals three relevant points. First, the reconstructed vibrational frequencies for the three main peaks due to the terminal methyl group of ODT are more accurate, and the modes exhibit narrower linewidths. Second, we identify spectral features that are not visible in the experimental spectrum, e.g., at 2845 cm^{-1} and 2950 cm^{-1}, which correspond to CH_2 stretching modes of ODT. Third, we find that the weak band around 2825 cm^{-1} in the spectrum is absent in reconstructed FID, as it is an artifact due to probing with an asymmetric pulse and should be interpreted as such.

To be able to reconstruct the complex polarization without being limited by the bandwidth of the probe or by the resolution of the spectrometer is an important advantage that needs to be verified via numerical simulations. For these simulations, we start with a single Lorentzian vibrational lineshape with a width of 1 cm^{-1} sampled on a grid of 4096 points with a spacing of 0.1 cm^{-1}. The probe before passing through the air-spaced étalon is a 100 fs pulse at 800 nm, and the delay increment is 150 fs. Figure 3(a) shows the reconstructed linewidth versus the total time window scanned with an ideal spectrometer resolution and a Fabry–Perot linewidth of 8 cm^{-1}. The longer the total scan window the better the match between reconstructed and original linewidths. Once the total time window is longer than the FID signal, the reconstructed linewidth is constant and equal to the original linewidth. In Fig. 3(b), the Fabry–Perot linewidth was scanned for a constant delay range of 100 ps and ideal spectrometer resolution. Up to approximately 25 cm^{-1}, the reconstructed linewidth matches the original. For larger values, the Fabry–Perot spacing becomes larger than the length of the laser pulse (100 fs) and the probe turns into a train of non-overlapping 100 fs pulses, which causes the reconstruction to fail. Figure 3(c) shows the reconstructed linewidth as a function of the spectrometer resolution for a constant delay range of 100 ps and a Fabry–Perot linewidth of 8 cm^{-1}. Up to

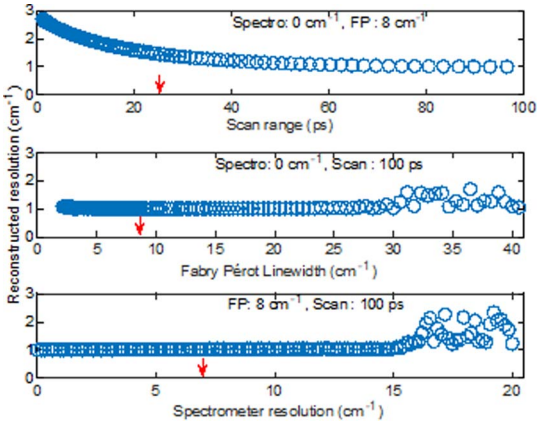

Fig. 3. Reconstructed linewidth as a function of (a) total scan range, (b) Fabry–Perot linewidth, and (c) spectrometer resolution. Red arrows indicate parameters used for the simulation in Fig. 4.

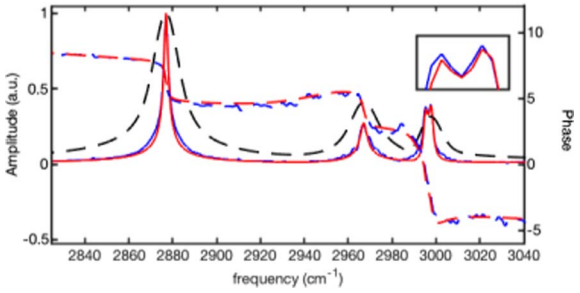

Fig. 4. Reconstructed (blue) and input (red) amplitude (solid curve) and phase (dashed curve). The inset shows a zoom to the double peak at 2990 cm^{-1} with a separation of 3 cm^{-1}. The black dashed line shows the square root of one of the simulated spectra.

about 30 cm^{-1}, the reconstruction is perfect; above this value, the spectral features blur out so much that the algorithm stops converging. Summarizing the results in Fig. 3 reveals that PIE reconstructs the true linewidth independent of the étalon and spectrometer resolution up to values that are 30 to 40 larger than the original linewidth.

For the set of parameters indicated by red arrows in Fig. 3 (probe linewidth: 8.6 cm^{-1}, spectrometer resolution: 7 cm^{-1}, and scan range: 25 ps), we simulate the reconstruction of a more complex system containing four vibrational modes with different amplitudes, phases, and linewidths. We used 30 spectra with a delay increment of 1 ps. The comparison of the reconstructed amplitude and phase with the original indicates excellent agreement, as seen in Fig. 4. For example, the reconstruction of the 1.8 cm^{-1} wide line results in a width of 1.9 cm^{-1}; the two lines separated by 3 cm^{-1} are very well resolved (inset in Fig. 4), and the reconstructed phase is also very accurate over the entire spectrum. We would like to stress that all features mentioned above are narrower than the probe linewidth as well as spectrometer resolution, as illustrated by the weakly resolved dashed line spectrum in Fig. 4. Recovering the true linewidth requires only acquiring data at long delays with a sufficiently high signal-to-noise ratio.

In conclusion, we introduced HIPPY, a new method for PS-SFG that does not require heterodyning and has a spectral resolution that is independent of probe bandwidth and spectrometer resolution. Only a few spectra measured at different time delays between IR and NIR pulses in a BB-vSFG configuration are required. Processing these spectra with the PIE algorithm allows to reconstruct the complex FID from the interface with a spectral resolution that is limited only by the maximum time delay. A NRB contribution can help reconstruction, but it is not a prerequisite to the application of HIPPY. The PIE is fast, robust, and easy to implement and can be applied to any coherent homodyne spectroscopy, in particular, coherent anti-Stokes Raman spectroscopy and transient grating spectroscopy.

Funding. Schweizerischer Nationalfonds zur Förderung der Wissenschaftlichen Forschung (NCCR-MUST); H2020 Marie Skłodowska-Curie Actions (801459, FP-RESOMUS); European Research Council (714586).

Disclosures. The authors declare no conflicts of interest.

See Supplement 1 for supporting content.

REFERENCES

1. Y. R. Shen, *Fundamentals of Sum-Frequency Spectroscopy* (Cambridge Core, 2016).
2. B. Busson and A. Tadjeddine, J. Phys. Chem. C **113**, 21895 (2009).
3. I. V. Stiopkin, H. D. Jayathilake, C. Weeraman, and A. V. Benderskii, J. Chem. Phys. **132**, 234503 (2010).
4. A. D. Curtis, M. C. Asplund, and J. E. Patterson, J. Phys. Chem. C **115**, 19303 (2011).
5. Y. R. Shen, Annu. Rev. Phys. Chem. **64**, 129 (2013).
6. A. L. Mifflin, L. Velarde, J. Ho, B. T. Psciuk, C. F. A. Negre, C. J. Ebben, M. A. Upshur, Z. Lu, B. L. Strick, R. J. Thomson, V. S. Batista, H.-F. Wang, and F. M. Geiger, J. Phys. Chem. A **119**, 1292 (2015).
7. W.-C. Yang and D. K. Hore, J. Chem. Phys. **149**, 174703 (2018).
8. L. Fu, S.-L. Chen, and H.-F. Wang, J. Phys. Chem. B **120**, 1579 (2016).
9. N. Ji, V. Ostroverkhov, C.-Y. Chen, and Y.-R. Shen, J. Am. Chem. Soc. **129**, 10056 (2007).
10. N. Ji, V. Ostroverkhov, C. S. Tian, and Y. R. Shen, Phys. Rev. Lett. **100**, 096102 (2008).
11. S. Yamaguchi and T. Tahara, J. Chem. Phys. **129**, 101102 (2008).
12. J. Wang, P. J. Bisson, J. M. Marmolejos, and M. J. Shultz, J. Phys. Chem. Lett. **7**, 1945 (2016).
13. H. Vanselous and P. B. Petersen, J. Phys. Chem. C **120**, 8175 (2016).
14. H. Wang, T. Gao, and W. Xiong, ACS Photon. **4**, 1839 (2017).
15. M. Thämer, R. K. Campen, and M. Wolf, Phys. Chem. Chem. Phys. **20**, 25875 (2018).
16. S. Sun, P. J. Bisson, M. Bonn, M. J. Shultz, and E. H. G. Backus, J. Phys. Chem. C **123**, 7266 (2019).
17. O. Isaienko and E. Borguet, Langmuir **29**, 7885 (2013).
18. O. Isaienko, S. Nihonyanagi, D. Sil, and E. Borguet, J. Phys. Chem. Lett. **4**, 531 (2013).
19. D. Spangenberg, P. Neethling, E. Rohwer, M. H. Brügmann, and T. Feurer, Phys. Rev. A **91**, 021803 (2015).
20. B. C. McCallum and J. M. Rodenburg, Ultramicroscopy **45**, 371 (1992).
21. M. Guizar-Sicairos, K. Evans-Lutterodt, A. F. Isakovic, A. Stein, J. B. Warren, A. R. Sandy, S. Narayanan, and J. R. Fienup, Opt. Express **18**, 18374 (2010).
22. D. Spangenberg, E. Rohwer, M. H. Brügmann, and T. Feurer, Opt. Lett. **40**, 1002 (2015).
23. M. Lucchini, M. H. Brügmann, A. Ludwig, L. Gallmann, U. Keller, and T. Feurer, Opt. Express **23**, 29502 (2015).
24. D.-M. Spangenberg, M. Brügmann, E. Rohwer, and T. Feurer, Appl. Opt. **55**, 5008 (2016).
25. T. Witting, D. Greening, D. Walke, P. Matia-Hernando, T. Barillot, J. P. Marangos, and J. W. G. Tisch, Opt. Lett. **41**, 4218 (2016).
26. P. Sidorenko, O. Lahav, Z. Avnat, and O. Cohen, Optica **3**, 1320 (2016).
27. M. Murari, M. Murari, G. D. Lucarelli, G. D. Lucarelli, M. Lucchini, M. Lucchini, M. Nisoli, and M. Nisoli, Opt. Express **28**, 10210 (2020).
28. J. E. Laaser, W. Xiong, and M. T. Zanni, J. Phys. Chem. B **115**, 2536 (2011).
29. L. Velarde and H.-F. Wang, Phys. Chem. Chem. Phys. **15**, 19970 (2013).
30. A. Lagutchev, S. A. Hambir, and D. D. Dlott, J. Phys. Chem. C **111**, 13645 (2007).
31. C. D. Bain, P. B. Davies, T. H. Ong, R. N. Ward, and M. A. Brown, Langmuir **7**, 1563 (1991).
32. J. Réhault, (2020) https://osapublishing.figshare.com/s/a3733a94fc8832869e07.
33. J. Réhault, (2020) https://osapublishing.figshare.com/s/e4c729d04b8cdbe89358.
34. S. Sun, R. Liang, X. Xu, H. Zhu, Y. R. Shen, and C. Tian, J. Chem. Phys. **144**, 244711 (2016).
35. P. E. Ohno, S. A. Saslow, H. Wang, F. M. Geiger, and K. B. Eisenthal, Nat. Commun. **7**, 1 (2016).
36. J. M. Marmolejos, P. J. Bisson, and M. J. Shultz, J. Chem. Phys. **150**, 124705 (2019).
37. H.-F. Wang, Prog. Surf. Sci. **91**, 155 (2016).
38. J. P. Kraack and P. Hamm, Chem. Rev. **117**, 10623 (2017).